# How Does Tunneling Contribute to Counterintuitive H-Abstraction Reactivity of Nonheme Fe(IV)O Oxidants with Alkanes?

Debasish Mandal, Rajeev Ramanan, Dandamudi Usharani,[†] Deepa Janardanan,[‡] Binju Wang, and Sason Shaik*

Institute of Chemistry and the Lise Meitner-Minerva Center for Computational Quantum Chemistry, The Hebrew University of Jerusalem, 91904 Jerusalem, Israel

S *Supporting Information*

ABSTRACT: This article addresses the intriguing hydrogen-abstraction (H-abstraction) and oxygen-transfer (O-transfer) reactivity of a series of nonheme $[Fe^{IV}(O)(TMC)(L_{ax})]^{z+}$ complexes, with a tetramethyl cyclam ligand and a variable axial ligand (L_{ax}), toward three substrates: 1,4-cyclohexadiene, 9,10-dihydroanthracene, and triphenyl phosphine. Experimentally, O-transfer-reactivity follows the relative electrophilicity of the complexes, whereas the corresponding H-abstraction-reactivity generally increases as the axial ligand becomes a better electron donor, hence exhibiting an antielectrophilic trend. Our theoretical results show that the antielectrophilic trend in H-abstraction is affected by tunneling contributions. Room-temperature tunneling increases with increase of the electron donation power of the axial-ligand, and this reverses the natural electrophilic trend, as revealed through calculations without tunneling, and leads to the observed antielectrophilic trend. By contrast, O-transfer-reactivity, not being subject to tunneling, retains an electrophilic-dependent reactivity trend, as revealed experimentally and computationally. Tunneling-corrected kinetic-isotope effect (KIE) calculations matched the experimental KIE values only if all of the H-abstraction reactions proceeded on the quintet state ($S = 2$) surface. As such, the present results corroborate the initially predicted two-state reactivity (TSR) scenario for these reactions. The increase of tunneling with the electron-releasing power of the axial ligand, and the reversal of the "natural" reactivity pattern, support the "tunneling control" hypothesis (Schreiner et al., ref 19). Should these predictions be corroborated, the entire field of C−H bond activation in bioinorganic chemistry would lay open to reinvestigation.
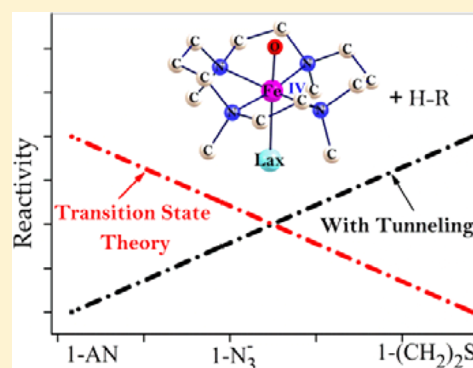
INTRODUCTION

Synthetic iron(IV)−oxo complexes serve as models for the active species of mononuclear nonheme iron enzymes[1−6] that currently captivate the interest of the chemical community because of their participation in important metabolic processes, neutralization of poisons, and DNA repair.[1] The many reactivity studies of these synthetic complexes toward C−H bond activation (eq 1) have created a variety of reactivity patterns.

$$LFe^{IV}=O + H-R$$
$$\rightarrow LFe^{III}-OH + R^{\bullet} \quad (L, \text{ a ligand system}) \qquad (1)$$
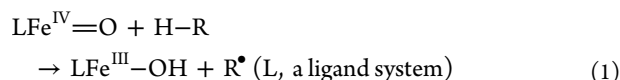
While some of these patterns are intuitively clear and follow the relative bond dissociation energy (BDE) of the C−H bonds undergoing activation or of the O−H bonds being made,[7−9] other patterns are counterintuitive.[10,11] Thus, for the series of the tetramethylcyclam (TMC) complexes, $[Fe^{IV}(O)(TMC)(L_{ax})]^{z+}$ ($z = 1, 2$), shown in Scheme 1a, where the iron(IV)−oxo is axially ligated by a variable axial ligand L_{ax} (**1**-AN, NCS^-, NCO^-, N_3^-, $CF_3CO_2^-$, $(CH_2)_2S^-$), the corresponding BDEs of the O−H bonds of the H-abstraction product were found to be virtually identical.[10,11] Because H-abstraction converts the iron(IV)−oxo moiety to iron(III)−hydroxo (eq 1), in the absence of the O−H
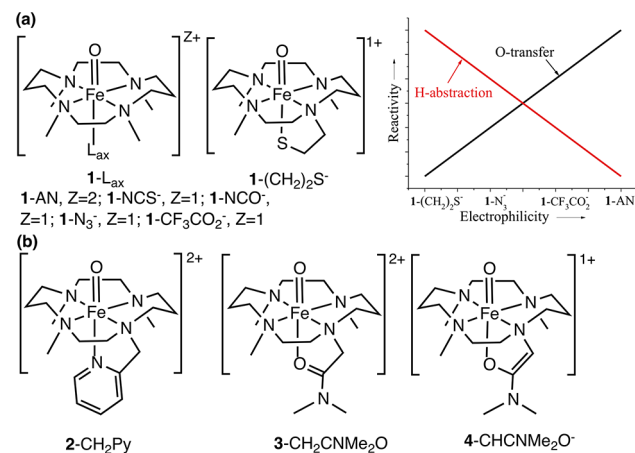
bond strength variation, it might have been expected that the reaction would follow the electrophilic power of the iron(IV)−oxo complexes, and exhibit a decreasing reactivity as the donor property of L_{ax} increases, thus rendering the most electrophilic complex, **1**-AN, also the most potent H-abstractor. Surprisingly, as shown by the reactivity cartoon in the right-hand side of Scheme 1a, the poorest electrophile with the strongest electron donor axial ligand, **1**-$(CH_2)_2S^-$, was found to be the most powerful H-abstractor, while the best electrophile, **1**-AN, was the least reactive; the rest of the ligands followed reactivity in the order of the electron releasing power of L_{ax}.[10,11] By contrast to this counterintuitive trend, the reactivity of the same set of the **1**-L_{ax} complexes in oxygen-transfer (O-transfer) reactions to phosphines (e.g., PPh_3) perfectly fitted the relative electrophilic power of the complexes, **1**-AN being the most reactive oxygenator.

How can one electrophilic reaction, H-abstraction, follow a trend that is basically opposite to the electrophilicity of the $[Fe^{IV}(O)(TMC)(L_{ax})]^{z+}$ bond activators, whereas at the same time, the O-transfer reactivity of the same complexes obeys their

Scheme 1. (a) $[Fe^{IV}(O)(TMC)(L_{ax})]^{z+}$ Complexes 1-L_{ax} and Their Relative Reactivity Patterns Shown on the Right-Hand Side Cartoon, in H-Abstraction from Alkanes (Red Line) and O-Transfer Reactions (Black Line) to Phosphines; (b) $[Fe^{IV}(O)(TMC)(L_{ax})]^{z+}$ Complexes 2-L_{ax}–4-L_{ax}, Which Deviate from the Behavior of 1-L_{ax} in (a)

Figure 1. Representation of the two-state reactivity (TSR) scenario during the H-abstraction reactions of a hexacoordinated iron(IV)−oxo complex with alkanes. ΔE_{TQ} is the energy gap between the triplet and quintet states, $^{3,5}TS_H$ are the respective transition states. $\Delta G^{\ddagger}$ is the free energy barrier from the ground state ^3R to ^5TS_H, and $^{3,5}I_H$ are the corresponding H-abstracted intermediate complexes. The same TSR scenario applies to O-transfer reactions to, for example, triphenylphosphines.

relative electrophilic character? This was a puzzle we encountered in 2007.[10]

One might have thought that the basicity of the ligand plays a role and stabilizes the H-abstraction transition states, as found recently in concerted proton coupled electron transfer (PCET) reactions of related and highly basic iron(IV)−oxo reagents.[12] However, our previous DFT calculations[11] showed that the barriers and the free energy barriers for both H-abstraction from 1,4-cyclohexadiene (CHD) and O-transfer to trimethyl or triphenyl phosphines decreased as the electrophilicity of the $[Fe^{IV}(O)(TMC)(L_{ax})]^{z+}$ complexes increased. This further exasperated the puzzle, so much so that we have begun doubting if DFT is at all capable of even qualitatively reproducing the experimental trends, let alone quantitatively. This suspicion subsided, however, when a solution presented itself by considering the two-state reactivity (TSR) that typifies these complexes (Figure 1).

Thus, like the majority of synthetic iron(IV)−oxo complexes, the $[Fe^{IV}(O)(TMC)(L_{ax})]^{z+}$ reagents[2,3,10] have a $S = 1$ (triplet) ground state and a low-lying $S = 2$ (quintet) excited state, and therefore the reactivity of the complexes involves TSR, as shown in Figure 1 for H-abstraction. The same TSR pattern applies to O-transfer reactions. As such, we reasoned[10,11] that because the reactions of these complexes involve spin crossover from the $S = 1$ ground state to the $S = 2$ transition state (TS), consequently, the barrier for the reaction was affected by both the energy gap between the two states (ΔE_{TQ}), as well as the spin-inversion probability (SIP) due to crossover from $S = 1$ to $S = 2$. It was plausibly argued and substantiated (see Figure S7 in the Supporting Information), by minimum energy crossing point (MECP) calculations,[13,14] that the SIP should be diminishing with the increase of the ΔE_{TQ} quantity, such that the most electrophilic reagent, 1-AN, with the highest ΔE_{TQ}, had the smallest spin inversion probability, while the least electrophilic reagent, 1-$(CH_2)_2S^−$, with the smallest ΔE_{TQ}, had the highest spin inversion probability (in 1-$(CH_2)_2S^−$, the sulfur may increase the SIP by its contribution to spin−orbit coupling). When this probability was incorporated, as a transmission coefficient in the Eyring equation, the order of H-abstraction reactivity could be inverted to the counterintuitive one in
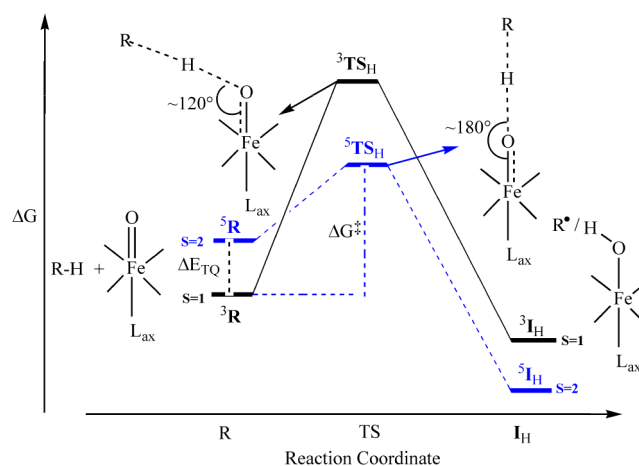
Scheme 1a, while the O-transfer reactivity continued to follow the relative electrophilicity of the complexes. This plausible modeling of the TSR reactivity received support from other iron(IV)−oxo studies,[11,13,15,16] and from studies of the analogous $[Ru^{IV}(O)(TMC)(L_{ax})]^{z+}$ complexes, where the reactivity involved only the $S = 1$ state, and which exhibited an electrophilicity controlled reactivity for both H-abstraction and O-transfer.[17]

Nevertheless, as the SIP values had to vary substantially across the series to reproduce the antielectrophilic experimental trend for H-abstraction, this explanation remained tentative. Recent experimental studies,[18] using the $[Fe^{IV}(O)(TMC)(L_{ax})]^{z+}$ complexes 1-AN and 2−4 in Scheme 1b, further challenged this interpretation. In this new series, 4 that has an anionic enolate (of a dimethyl acetamido moiety) as axial ligand is the least electrophilic, 2 that has a tethered pyridine (Py) ligand is the most electrophilic, while 3 in which the neutral dimethyl acetamido serves as ligand has an intermediate electrophilicity. This series exhibited a normal O-transfer reactivity order, 1-AN $\geq$ 2 > 3 > 4, which obeyed the relative electrophilicity order. However, the H-abstraction reactivity trend did not fit the original pattern of the 1-L_{ax} series. Thus, whereas the complex 1-$(CH_2)_2S^−$ having the most electron-donating ligand was also the most highly reactive H-abstractor in the original 1-L_{ax} series, by contrast, in the new series, the 4-$CHCNMe_2O^−$ complex, wherein the axial ligand appears to be an equally powerful electron donor, was the least reactive. Consequently, we are now facing an even more intriguing puzzle that needs a better solution than before.

How can we account for the curious reactivity patterns in the entire H-abstraction by the $[Fe^{IV}(O)(TMC)(L_{ax})]^{z+}$ complexes? Because the earlier experimental study[10] indicated that some of the reactions exhibited quite high kinetic isotope effect (KIE) values, higher than the accepted classical limit (7−8), we have decided to reinvestigate these systems with inclusion of tunneling that was not considered in the original[11] modeling. Indeed, the recent work of Schreiner et al. showed that tunneling could drive

counterintuitive reaction selectivities, termed by Schreiner as "tunneling control".[19]

The reactions that we investigated herein are enumerated in Scheme 2. They involve a family of five iron(IV)−oxo complexes

Scheme 2. Studied H-Abstraction and O-Transfer Reactions between Iron(IV)−Oxo Reagents $[Fe^{IV}(O)(TMC)(L_{ax})]^{z+}$ and Different Substrates[a]
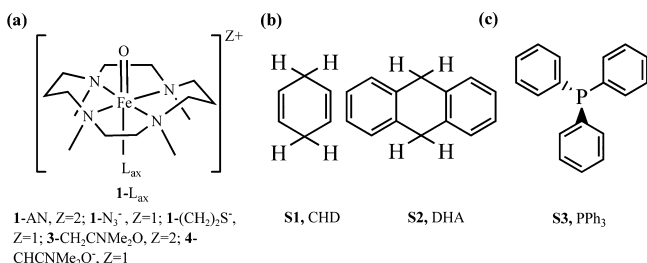
[a] (a) The iron(IV)−oxo reagents, **1**-L_{ax}, **3**, and **4**. (b) Substrates **S1** and **S2** for H-abstraction reactions. (c) **S3** used for the study of O-transfer from **1**-AN, **1**-$(CH_2)_2S^−$, **3**, and **4**.

and two substrates, cyclohexadiene (CHD, **S1**) and 9,10-dihydroanthracene (DHA, **S2**), which have been used in the experiment and underwent H-abstraction.[10,18] The use of **S2** in addition to **S1**, despite their similar BDE(C−H) values, was deemed essential because the superior H-abstraction capability of **1**-$(CH_2)_2S^−$ was demonstrated in the original experimental study[10] by comparing the reactions of **1**-AN and **1**-$(CH_2)_2S^−$ with **S2**, and not with **S1**. Further, to have reference reactions that do not involve tunneling effects, we studied the O-transfer reactions of the oxidants to PPh_3 (**S3**).

As we shall demonstrate, the inclusion of tunneling correction in the H-abstraction reactions leads to two main conclusions: the tunneling correction conserves the TSR reactivity scenario, and, at the same time, the correction increases as the ligand's electron-donating ability improves. Consequently, the tunneling creates the antielectrophilic reactivity pattern in the H-abstraction reactions of **1**-L_{ax} with **S1** and **S2**. At the same time, tunneling still conserves the recently observed[18] electrophilic trend in the relative reactivities of **1**-AN, **3**, and **4** with **S1**. By contrast, the O-transfer reactions of **1**-AN and **1**-$(CH_2)_2S^−$ to PPh_3 (**S3**) exhibit the original electrophilicity controlled reactivity, because they are not subject to tunneling. Some predictions will be discussed, for example, the finding that the tunneling corrected KIE is a probe of the reactive spin state. Generalizations follow about the patterns of electrophilic reactivity of iron(IV)−oxo reactions.

■ COMPUTATIONAL DETAILS

In the original theoretical study,[11] where we did not use counterions for the positively charged iron(IV)−oxo reagents, the gas-phase barrier on the $S = 2$ surface was underestimated. Thus, for example, for **1**-AN reacting with **S1**, the $S = 2$ barrier altogether vanished and the reaction intermediate (^5I_H, Figure 1) was a carbocation, and/or the process resulted in electron transfer.[11,20] In other cases, the imaginary frequency (which is crucial in tunneling correction) was seriously underestimated. It was argued that such artificial phenomena reflected the self-interaction errors (SIEs) in DFT.[21] Our recent detailed study of the $[Fe^{IV}(O)-N4Py]^{2+}$ complex showed that usage of counterions to neutralize the charge of the oxidants caused all of these artificial phenomena to vanish.[20] The alternative way to rid of SIE employs solvent phase geometry optimization. However, as we showed in ref 20, this approach still leads to formation of a carbocation intermediate with **S1**.Therefore, to avoid these effects, here we neutralized the charge of the iron(IV)−

oxo reagents with triflate ($CF_3SO_3^−$) counterions. Geometry optimizations were conducted with UB3LYP.[22−24] For all of the species, we used the LACVP*(Fe)/6-31G*(rest) basis set,[25,26] labeled B1a, while for **1**-AN and **1**-$(CH_2)_2S^−$ reacting with **S2** (DHA) we also tested the effect of the all-electron split-valence polarized Def2-SV(P) basis set,[27] labeled B1b, on the geometry.

Geometry optimization at the B1a and B1b level of theory was carried out with the Jaguar 7.6[28] and Gaussian 09[29] program packages, respectively. A subsequent frequency calculation was also done at the same level to confirm the nature of the optimized structures as local minima (no imaginary frequency) or transition states (one imaginary frequency), and to evaluate the zero-point vibrational energy (ZPVE), as well as thermal and entropic corrections to the Gibbs free energy at $T = 273$ K (0 °C), which is the experimental temperature.[10] The energies were further corrected with two larger basis sets, LACV3P+*(Fe)/6-311+G*, labeled B2, and the all electron Def2-TZVPP[30] basis set, labeled B3. Solvent-effect corrections on B1a geometries were carried out at the B2 level with the Poission−Boltzman solvation (PBS) model[31] in Jaguar,[28] using a dielectric constant (ε) of 37.5 (acetonitrile) and a probe radius of 2.183. The solvent corrections have also been performed at the B3/B1b level using PCM model with the default UFF radii in Gaussian 09 on the B1b geometry.

The various combinations of energies are labeled as E_{el}, E, and G (all with solvation correction), where E_{el} is the solvation-corrected electronic energy, E refers to the solvent- and ZPVE-corrected energy, while G involves also the thermal and entropy corrections and hence corresponding free energies. Because there are various basis set combinations, we specify these in parentheses; for example, $E(B3//B1a)$ would involve the B3//B1a energy with solvent and the ZPVE corrections, $G(B3//B1a)$ will signify the corresponding free energy (see the Supporting Information for the details of abbreviations), etc. Common levels for all of the reactions studied here are $E(B3//B1a)$ and $G(B3//B1a)$. In addition to the UB3LYP functional, we tested also UTPSSh,[32a] as well as UM06-L[32b] and UOPBE,[32c,d] and the SMD solvation model.[32e] With all of these functionals and SMD, we used only single-point B3 energies on the UB3LYP geometries, and, in addition, for UTPSSh we used also B1a optimization. The UB3LYP results, at the common uniform level, are discussed in the text; the other results are mentioned in brief (Table 2). All of these results are reported in the Supporting Information.

Spin densities, Mulliken charges, natural, and Kohn−Sham orbitals were analyzed for the correct identification of electronic state. Dispersion corrections have been calculated in the Grimme's DFT-D3 program.[33] These data are relegated to the Supporting Information.

Electron Donation Index of the Axial Ligands. To gauge the electron donation ability of the various axial ligands, we calculated the amount of charge transferred from the axial ligand to the $[Fe^{IV}(O)-(TMC)]$ moiety, Δq_{CT}. This quantity was determined from the difference of the charge of the axial ligand in the oxidant, in $S = 2$, vis-à-vis its native charge as a free ligand (−1 for anionic ligands, e.g., $(CH_2)_2S^−$, and zero for neutrals, e.g., AN). The calculations used both natural bond orbital (NBO) and simple Mulliken populations at the LACV3P+* basis set. The two sets of Δq_{CT} quantities matched very well, and the match extended to the gas-phase values calculated[11] for these complexes devoid of counterions. This shows that the counterion does not affect this property of the isolated oxidant (while affecting the TSs and intermediates of the reactions). Thus, the more negative is the Δq_{CT}, the more charge is transferred from the axial ligand to the reaction center, and the less electrophilic becomes the iron(IV)−oxo complex.

Tunneling Corrections and Kinetic Isotope Effect (KIE) Calculations. One-dimensional models generally underestimate the tunneling correction for polyatomic molecules, because these models are restricted to the adiabatic minimum energy pathway (AMEP) and do not take advantage of alternative paths (e.g., by corner cutting), which augment the tunneling effect.[34,35] Nevertheless, it was found in a few studies of H-transfer/migration reactions of polyatomic molecules[36−38] that the Eckart model exhibits a reasonable agreement with the more sophisticated multidimensional tunneling methods, which include corner cutting (e.g., the SCT method). Our approach is therefore pragmatic, in the sense that we are looking at the trend of the tunneling
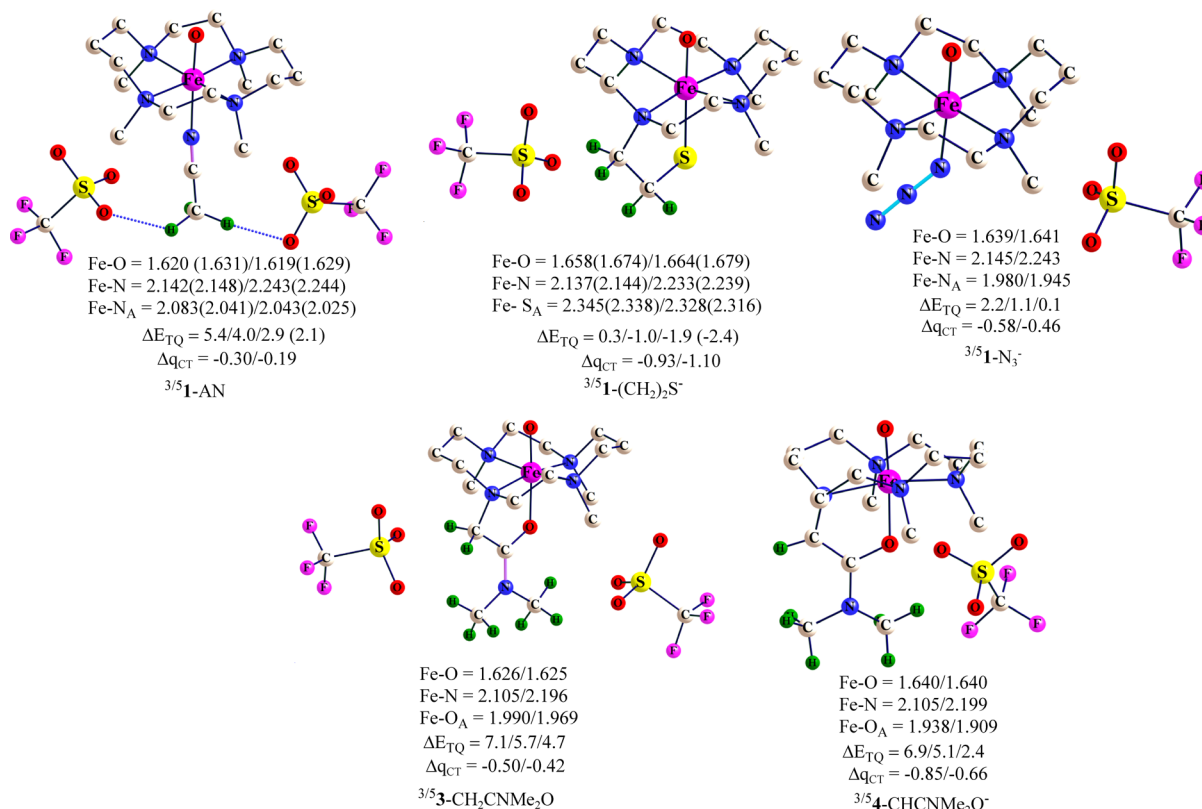
Fe-O = 1.620 (1.631)/1.619(1.629)
Fe-N = 2.142(2.148)/2.243(2.244)
Fe-N$_A$ = 2.083(2.041)/2.043(2.025)
ΔE_{TQ} = 5.4/4.0/2.9 (2.1)
Δq_{CT} = -0.30/-0.19
$^{3/5}$**1**-AN

Fe-O = 1.658(1.674)/1.664(1.679)
Fe-N = 2.137(2.144)/2.233(2.239)
Fe- S$_A$ = 2.345(2.338)/2.328(2.316)
ΔE_{TQ} = 0.3/-1.0/-1.9 (-2.4)
Δq_{CT} = -0.93/-1.10
$^{3/5}$**1**-(CH$_2$)$_2$S$^-$

Fe-O = 1.639/1.641
Fe-N = 2.145/2.243
Fe-N$_A$ = 1.980/1.945
ΔE_{TQ} = 2.2/1.1/0.1
Δq_{CT} = -0.58/-0.46
$^{3/5}$**1**-N$_3$$^-$

Fe-O = 1.626/1.625
Fe-N = 2.105/2.196
Fe-O$_A$ = 1.990/1.969
ΔE_{TQ} = 7.1/5.7/4.7
Δq_{CT} = -0.50/-0.42
$^{3/5}$**3**-CH$_2$CNMe$_2$O

Fe-O = 1.640/1.640
Fe-N = 2.105/2.199
Fe-O$_A$ = 1.938/1.909
ΔE_{TQ} = 6.9/5.1/2.4
Δq_{CT} = -0.85/-0.66
$^{3/5}$**4**-CHCNMe$_2$O$^-$

Figure 2. UB3LYP/B1a optimized geometries with geometrical parameters (distances in Å, angles in degrees), ΔE_{TQ} (in kcal mol^{-1}), and Δq_{CT} (in e$^-$ units) for all of the oxidants. Fe−N corresponds to the average distances between Fe and the four equatorial N atoms. Fe−N$_A$/S$_A$/O$_A$ represents distances between Fe and the axial nitrogen/sulfur/oxygen atom. Only selected H atoms are shown for clarity. The Δq_{CT} values are presented as Mulliken/NBO calculated at B2//B1a level. The ΔE_{TQ} values are presented as follows: E_{el}(B2//B1a)/E(B3//B1a)/G(B3//B1a); E_{el} is the electronic energy with solvation correction. The geometrical parameters and ΔE_{TQ} values given in parentheses for **1**-AN and **1**-(CH$_2$)$_2$S$^-$ are calculated at the UB3LYP/B1b and G(B3//B1b) levels, respectively.

correction in a series of reactions, with the understanding that the effect may be a lower limit of a more accurate tunneling correction.[34b,39] Thus, as our reaction set is large and the systems have around 80 atoms each, and as the Eckart method requires less computational effort, we use it herein.

Eckart tunneling calculations were performed using TheRate program.[40] The Eckart-based method uses an analytical potential energy function fitted by the computed and ZPVE (and solvent) corrected energies of the reactants, products, and TS, as well as the imaginary frequency along the AMEP, that is, the intrinsic reaction coordinate (IRC), in mass weighted coordinates.[41a,b] Using the definitions in this Article, the Eckart function is fitted at the E level. The transmission coefficient, κ, due to tunneling is calculated by integration of the barrier "penetration" probability as a Boltzmann-averaged function of the energy.[41a] The effect of the transmission coefficient κ on the barrier is calculated by the following equation:

$$\Delta\Delta E^{\ddagger}_{tun} = -RT \ln \kappa(T) \qquad (2)$$

Here, R is the universal gas constant and T is the absolute temperature. As can be seen from eq 2, the tunneling correction effectively cuts the barrier by the quantity $\Delta\Delta E^{\ddagger}_{tun}$. This correction, which corresponds to the E level, was applied also to the free energy barriers at the G level.

Corresponding kinetic isotopic effects (KIEs) were calculated for all of the reactions, and compared to available experimental data[10] to ascertain the reliability of the tunneling contribution. The KIE calculations employed the frequencies of the reaction of the iron-(IV)−oxo complexes with CHD and DHA and their deuterated isotopomers. The KIEs were calculated using the semiclassical Eyring equation,[42] followed by tunneling corrected (TC) values, using the following expression:

$$KIE_{TC} = (\kappa_H/\kappa_D)\cdot KIE_{EY} \qquad (3)$$

where κ_H/κ_D is the transmission coefficients of the two isotopomers, evaluated by the Eckart method. For comparison, we also tested the tunneling effect using the Wigner[43] method, which highly under-estimates tunneling.

Because the experimental rate data were collected at 273 K while the KIE data were measured at 298 K, in the following discussion we present barriers and transmission coefficient at 273 K and KIE at 298 K unless otherwise mentioned.

RESULTS AND DISCUSSION

Iron(IV)−Oxo Complexes. The optimized iron(IV)−oxo reagents are depicted in Figure 2 along with key geometric parameters, Δq_{CT} and ΔE_{TQ} quantities. Scheme 3 displays in addition to the Δq_{CT} quantities also the lowest unoccupied MOs (LUMOs) and their energies for the corresponding complexes at the S = 2 state. The following trends are noted:

(a) The counterions are nestled near the bottom parts of the axial ligands. As in the previous study,[20] these positions of the counterions remain unaltered during the geometry optimization of the species along the reaction coordinate.

(b) UB3LYP shows that the ΔE_{TQ} gaps decrease, as the axial ligand becomes a better electron donor. The lowest ΔE_{TQ} gap corresponds to **1**-(CH$_2$)$_2$S$^-$ in accord with conclusions derived from Mössbauer spectroscopic data.[44] Upon adding solvation, ZPVE, and thermal corrections, the quintet state of **1**-(CH$_2$)$_2$S$^-$ becomes the ground state. Still, the S = 2 and S = 1 states remain virtually degenerate.

Scheme 3. The Lowest Unoccupied Molecular Orbitals (LUMOs) for the Oxidants in $S = 2$, Their Energies (in eV) Calculated at the UB3LYP/B1a Level of Theory, and Δq_{CT} in the Order of Mulliken/NBO for All of the Oxidants
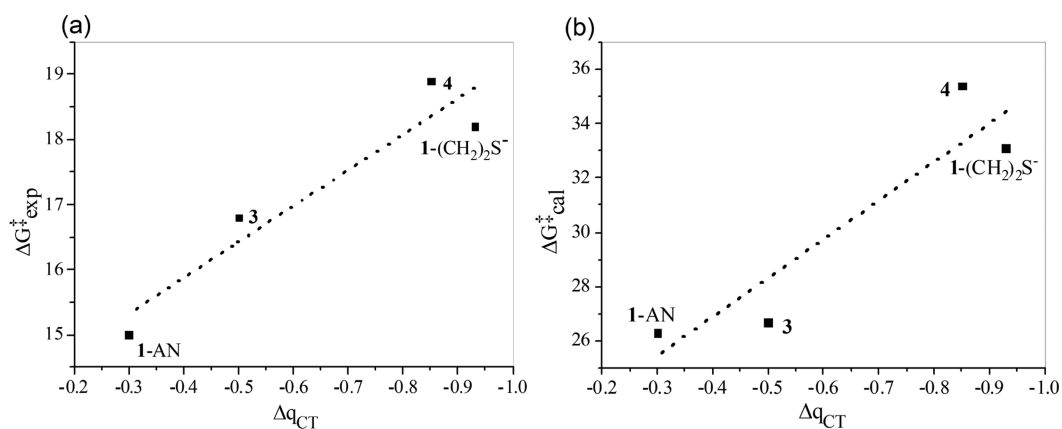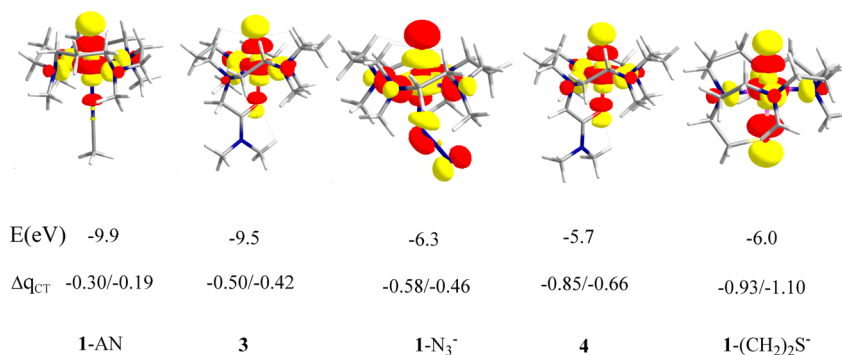
E(eV) -9.9	-9.5	-6.3	-5.7	-6.0
Δq_{CT} -0.30/-0.19	-0.50/-0.42	-0.58/-0.46	-0.85/-0.66	-0.93/-1.10
1-AN	**3**	**1-N$_3^-$**	**4**	**1-(CH$_2$)$_2$S$^-$**

Figure 3. Plots of free energy barriers for O-transfer reactions to **S3** versus the electrophilicity parameter, Δq_{CT}, of the axial ligand in the iron(IV)−oxo complexes: (a) experimental $\Delta G_{exp}^{\ddagger}$ data; (b) computed $\Delta G_{cal}^{\ddagger}$(B2//B1a) at 273 K for $S = 2$.
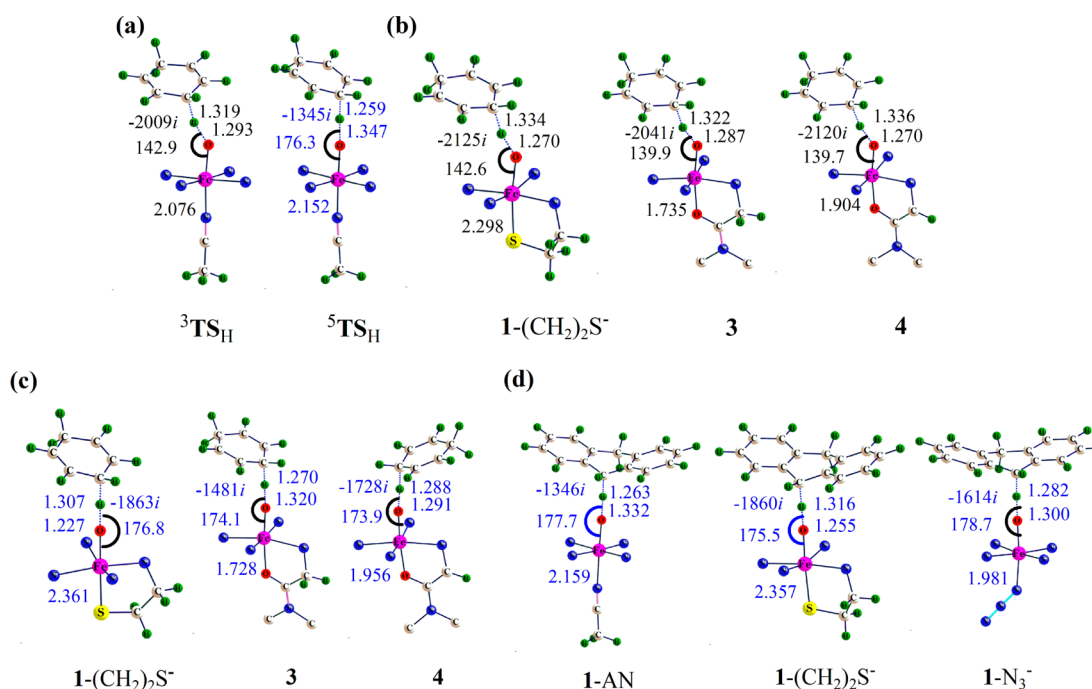

Figure 4. UB3LYP/B1a optimized transition state structures (distances in Å and angles in degrees) and imaginary frequencies (in i cm^{-1}) for H-abstraction in the triplet and quintet spin states (^{3,5}TS$_H$): (a) The ^{3,5}TS$_H$ structures for the reaction of **1-AN** with **S1**(CHD). (b) Geometric features of the Fe−O---H---R moieties for the ^{3}TS$_H$ structures for **1**-(CH$_2$)$_2$S$^-$, **3**, and **4**, reacting with **S1** (CHD). (c) Geometric features of the Fe−O---H---R moieties for the ^{5}TS$_H$ structures for **1**-(CH$_2$)$_2$S$^-$, **3**, and **4**, reacting with **S1** (CHD). (d) Geometric features of the Fe−O---H---R moieties for the ^{5}TS$_H$ structures for **1**-L$_{ax}$ oxidants reacting with **S2** (DHA). For the sake of clarity, the counterions are omitted and the coordination center of iron is simplified.

Interestingly, the quintet states of **3** and **4** are relatively high lying as compared to the other oxidants.

(c) For **1**-AN and **1**-$(CH_2)_2S^-$, which were tested with both B1a and B1b, the geometries are not significantly affected in the two different basis sets.

(d) Inspection of the Δq_{CT} quantities shows that the L_{ax} = AN ligand is the least electron releasing ligand, while L_{ax} = $(CH_2)_2S^-$ is the most powerful electron releasing ligand. As such, the electrophilicity of the various complexes decreases in the following order: **1**-AN > **3** > **1**-N_3^- > **4** > **1**-$(CH_2)_2S^-$.

(e) Inspection of Scheme 3 reveals that, as expected, the LUMO for the $S = 2$ state is the $\sigma^*_{z^2}$ orbital for all of the complexes. Furthermore, the LUMO energies (in the $S = 2$ states) increase (become less negative) as the axial ligand becomes a better electron donor. Thus, **1**-AN, the best electrophile, has the lowest LUMO and the least negative Δq_{CT}, while **1**-$(CH_2)_2S^-$ and **4** have the highest LUMOs and the most negative Δq_{CT}.

O-Transfer Reactions. As discussed previously,[11] O-transfer reactions are "two-electron reactions", in which one electron from the phosphine lone-pair orbital is shifted to the $\sigma^*_{z^2}$ orbital in both spin states, while the second electron shifts to lower-lying $\pi^*_{xz/yz}$ and δ orbitals. Because the $\sigma^*_{z^2}$ orbital is oriented along the L_{ax}−Fe−O axis, the geometries of the corresponding transition states ($^{3,5}TS_O$) show a propensity to assume an upright orientation with FeOP angles >150°. These structures are collected in the Supporting Information in Figure S1.

The reactivity of the various iron(IV)−oxo complexes toward **S3** (PPh₃) follows their relative electrophilicity. Thus, as shown in Figure 3a and b, the experimental free energy barriers (Figure 3a) and the theoretical barriers, at the $\Delta G_{cal}^{\ddagger}$(B2//B1a) level, follow basically the order of the Δq_{CT} quantities. Thus, the most powerful electrophile **1**-AN has the lower barrier, while **1**-$(CH_2)_2S^-$ and **4**, which are the poorest electrophiles, possess the highest barriers. As such, DFT reproduces the experimentally observed trend[10,18] that electrophilicity of the iron(IV)−oxo reagents dominates their O-transfer reactivity.

H-Abstraction Reactions. The geometries of the transition states for H-abstraction ($^{3,5}TS_H$) and the corresponding reaction intermediates are depicted in Figures S2 and S3 of the Supporting Information. Because the TS structures are rather typical, we present representative structures. Figure 4a shows a pair of structures for **1**-AN + **S1** (CHD) in the $S = 1$ and $S = 2$ TSs, while in Figure 4b and c we show $S = 1$ and $S = 2$ TSs, respectively, for other oxidants reacting with **S1** (CHD). Figure 4d shows the $S = 2$ TSs for the reaction of the latter oxidants with **S2** (DHA). Scheme 4 shows the orbital interactions that control the structures of these TSs with respect to the relative orientation of the iron(IV)−oxo complex and the hydrocarbon.

The following trends are noted by inspection of Figure 4 and Scheme 4:

(a) The TSs in Figure 4 follow the previously discussed orbital selection rules.[45−51] Thus, as shown in the cartoons in Scheme 4, the ^3TS_H species follows the π^* trajectory and have as such a sideways structure with an FeOH angle of approximately 120°. On the other hand, the ^5TS_H species follow the $\sigma^*_{z^2}$ trajectory, and are therefore upright with an FeOH angle of approximately 180° shown in Scheme 4b. The deviation from these angles in ^3TS_H may reflect the response to steric effects.[51]

Scheme 4. Electron-Shift Diagrams[13,16,45] and Orbital-Overlap Cartoons Showing the Orbital Interactions That Control the Shape of the $^{3,5}TS_H$ Structures[a]
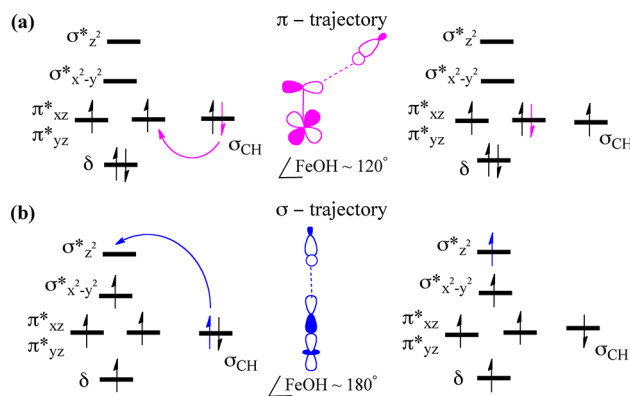
[a]The shape of the ^3TS_H species is dominated by the overlap of the $\pi^*_{xz/yz}$ and σ_{CH} orbitals, while the corresponding ^5TS_H species is dominated by the overlap of the $\sigma^*_{z^2}$ and σ_{CH} orbitals.

(b) The C---H and O---H distances in $S = 1$ and $S = 2$ show that the C---H bond length decreases in the order **1**-$(CH_2)_2S^-$ > **4** > **3** > **1**-AN and **1**-$(CH_2)_2S^-$ > **1**-N_3^- > **1**-AN, whereas the H---O distance increases in the order **1**-$(CH_2)_2S^-$ < **4** < **3** < **1**-AN and **1**-$(CH_2)_2S^-$ < **1**-N_3^- < **1**-AN. Thus, **1**-AN has the most "reactant-like" TS, with less C---H bond cleavage and less O---H bond formation, whereas **1**-$(CH_2)_2S^-$ exhibits the most "product-like" TS with the highest degrees of C---H cleavage and O---H formation. Generally, the TSs for the $S = 1$ state involve higher degrees of C---H bond cleavage and O---H bond formation, as compared to the $S = 2$ species, and hence the corresponding barriers are larger for $S = 1$.

(c) Considering the O---H----C distances in Figure 4, we can see that **1**-$(CH_2)_2S^-$ has the shortest O---C distance and it is the "tightest" TS, while **1**-AN has the "loosest" TS. This trend matches the corresponding one in the imaginary frequencies, being largest for **1**-$(CH_2)_2S^-$ and smallest for **1**-AN. The imaginary frequency affects the width of the barrier; the larger it is, the narrower is the barrier. This will be crucial for the tunneling correction. As we shall see immediately, these trends reflect the relative barriers for the various oxidants.

Before proceeding to consider the barriers for the reactions, let us reiterate that the barriers for the $S = 1$ state are substantially higher than those for the $S = 2$ state,[13,16,45,49] in accord with the fundamental rule of exchange-enhanced reactivity.[13,16,52] This situation is not altered by the tunneling corrections (all of the barriers are relegated to the Supporting Information; see Table S3, Figure S4). Therefore, we may conclude that all of the H-abstraction reactions exhibit TSR and pass via the $S = 2$ surface, as depicted schematically in Figure 1. Later, we show that this statement is in fact experimentally supported.

Figure 5 shows the trends in the computed free energies of activation (uncorrected yet by tunneling) and the experimental quantities against the electrophilicity index Δq_{CT}. The doubling of the points for some of the oxidants corresponds to H-abstraction barriers for reactions with both **S1** (●) and **S2** (red ◆). The dashed lines connecting the data points (in part a) and passing between the points (in part b) are drawn to guide the eye. In Figure 5a, black and red dotted lines follow the
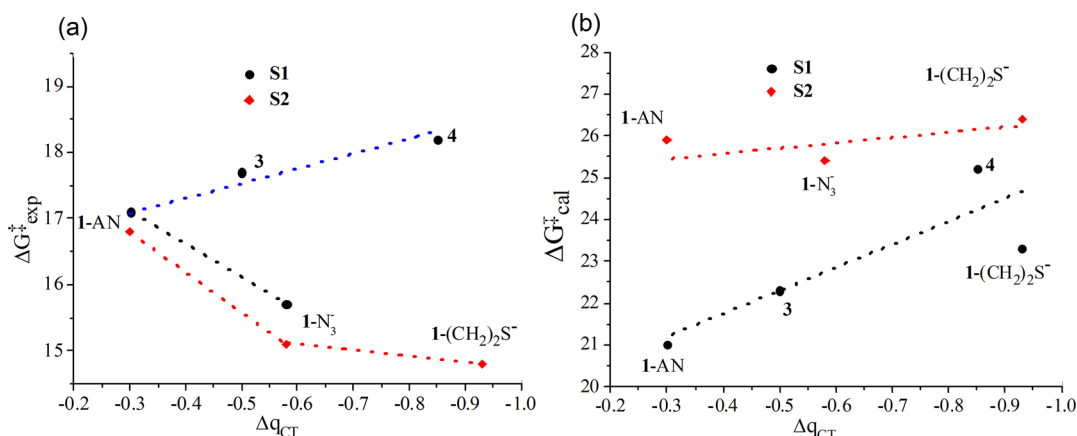
Figure 5. Free energy barriers, for the reaction of the various oxidants with **S1** (CHD) and **S2** (DHA), plotted against the Δq_{CT} indices of the oxidants: (a) Experimental barriers. (b) Theoretical UB3LYP quintet-state barriers at the G(B3//B1a) level. The reactions with **S1** are indicated by the "●", while those with **S2** by red "◆".

antielectrophilic trend of reactivity, whereas the blue dotted line follows the opposite trend.

It is seen that the computational barriers in Figure 5b increase as the electron releasing power of the axial ligand increases; the least electrophilic iron(IV)−oxo complexes, 1-$(CH_2)_2S^-$ and **4**, have the highest barriers, while the best electrophile **1-AN** has the smallest barrier. This trend is common to all of the energy levels E_{el}, E, and G. It follows also from the relative LUMO energies of these complexes in Scheme 3.[49] The same trend was also found in CCSD(T) calculations of model systems,[13b,53a] which revealed that an electron-donating axial ligand raises the H-abstraction barrier, and that the UB3LYP barriers correlate well with the CCSD(T) barriers. It is clear that the UB3LYP computed trend in the classical barrier is physically sound and will likely survive the test by reliable first-principle methods like CCSD(T).[53b] By contrast, as can be seen in Figure 5a, the experimental barriers for the reactions of 1-L_{ax} with either **S1** or **S2** get lower as the complex becomes less electrophilic, and for **S2** is the lowest for 1-$(CH_2)_2S^-$ and highest for **1-AN**.[10] The rest of the barrier data (for **S1** activation) varies in the order **1-AN** < **3** < **4**, which approximately matches the electrophilicity.[18]

Considerations of Tunneling Corrections of the Barriers for H-Abstraction. Clearly, by contrast to the O-transfer reactions (Figure 3), for the H-abstraction reactions (Figure 5) there is a mismatch between the trends of the experimental and theoretical barriers. It is important to emphasize here that the reaction energies of these various reactions (with **S1**) are virtually the same, and so are the O−H bond dissociation energies (BDEs) of the iron(III)−OH product complexes (see Supporting Information Table S5). As such, the Bell−Evans−Polanyi (BEP) principle[54,55] does not apply to either the experimental trends or the theoretical ones. So, what could be the factor that produces the observed experimental trend?

Because H is a small particle subject to quantum mechanical tunneling, and because the available experimental data reveal KIE values[10] that are indicative of tunneling, that is, ≥10, we consider now the effect of tunneling on the effective barrier of the reaction, using the simplified representation as shown in Scheme 5. Thus, the tunneling "through" the barrier[19] reduces it by a quantity $\Delta\Delta E^{\ddagger}_{tun}$, which depends on the transmission coefficient as specified above in eq 2. The outcome is that the H-abstraction transpires with an effective barrier $\Delta E^{\ddagger}_{eff}$ that is smaller than the semiclassical barrier $\Delta E^{\ddagger}$.

Scheme 5. A Schematic Cartoon of a Barrier along the Reaction Coordinates^a
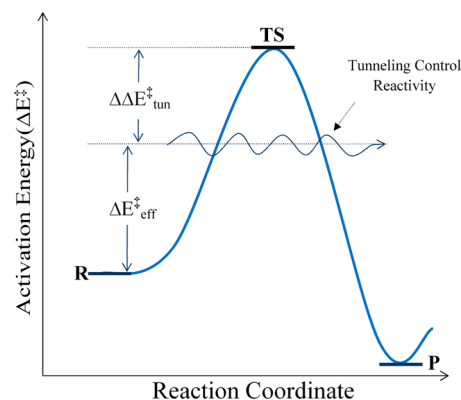
^{a}The tunneling (wavy arrow) occurs below the transition state, cutting the barrier by $\Delta\Delta E^{\ddagger}_{tun}$ and producing an effective barrier $\Delta E^{\ddagger}_{eff}$ that is smaller than the semi-classical one.

As we already noted, the $S = 1$ barriers are higher than those for $S = 2$ before and after tunneling correction (Supporting Information Table S3), and therefore we consider only the quintet state ($S = 2$) reactions. To assist with the discussion of the tunneling trends for the various H-transfer reactions, we collected in Tables 1 and 2 necessary data for the discussion. Figures 6−8 further provide pictorial presentations of the trends in Table 1.

Thus, Table 1 displays the imaginary frequency for the ^5TS_H species, the transmission coefficients for H tunneling using the Eckart model, and the values of $\Delta\Delta E^{\ddagger}_{tun}$ and $\Delta E^{\ddagger}_{eff}$ at the common levels, E(B3//B1a) and G(B3//B1a), where the former is the ZPVE corrected quantity and the latter is the free energy, both including solvent corrections. Because the reaction energy is also important for tunneling (highly exo- and endothermic reactions reduce the energy span for tunneling), we report also ΔE_{rp}(B3//B1a) values for the various reactions. Where available we show in parentheses $\Delta\Delta E^{\ddagger}_{tun}$ entries that correspond to the B1b geometry optimization levels.

Inspection of the $\Delta\Delta E^{\ddagger}_{tun}$ quantities in entries (a) and (b) in Table 1 shows that the tunneling cuts the quintet barrier by substantial amounts, which depend on the electron-donating power of the axial ligand, Δq_{CT}. Thus, as Δq_{CT} becomes more

Table 1. Imaginary Frequencies at UB3LYP/B1a, the Transmission Coefficients for H-Tunneling at 273 K, Reaction Energies, ΔE_{rp}, Barrier Lowering Quantities ($\Delta\Delta E^{\ddagger}_{tun}$) Due to Tunneling at E(B3//B1a), and the Quintet-State Effective Barriers $\Delta E^{\ddagger}_{eff}$ at E(B3//B1a) and G(B3//B1a) Levels

reaction[a]	$\nu_H^{\ddagger}$	κ_H	ΔE_{rp}[b]	$\Delta\Delta E^{\ddagger}_{tun}$ E(B3//B1a)	$\Delta E^{\ddagger}_{eff}$ E(B3//B1a)	$\Delta G^{\ddagger}_{eff}$ G(B3//B1a)
(a) S = 2 (CHD)						
1-AN	1346	13	−10.0	1.4 (1.0)	10.7	19.6
1-(CH$_2$)$_2$S$^-$	1863	502	−11.1	3.4 (2.9)	9.6	19.9
3	1482	20	−9.6	1.6	11.5	20.7
4	1728	195	−8.0	2.9	14.7	22.4
(b) S = 2 (DHA)						
1-AN	1346	16	−5.7	1.5 (1.2)	12.6	24.4
1-(CH$_2$)$_2$S$^-$	1860	617	−1.9	3.5 (3.1)	11.6	22.9
1-N$_3^-$	1614	93	−7.1	2.4	11.4	23.0

[a]The energies are in kcal mol^{-1} and $\nu_H^{\ddagger}$ is in i cm^{-1}. [b]ΔE_{rp} stands for $E_{product} − E_{reactant}$ and reactant is in the ground state. The $\Delta\Delta E^{\ddagger}_{tun}$ values given in parentheses are the corresponding values for the B1b structures.

negative, the $\Delta\Delta E^{\ddagger}_{tun}$ increases from 1.2 to 1.5 kcal mol^{-1} for **1**-AN all of the way to 3.1−3.5 kcal mol^{-1} for **1**-(CH$_2$)$_2$S$^-$. Figure 6a shows this trend pictorially for all of the oxidants.

As shown in Table 2, the trend in the tunneling correction $\Delta\Delta E^{\ddagger}_{tun}$ is invariant, and does not depend on the basis-set, functional and solvent model (see also Supporting Information Tables S4, S7). In all cases, the tunneling correction for **1**-(CH$_2$)$_2$S$^-$ is larger than that for **1**-AN.

The outcome of this barrier cutting is that the trend in the effective barriers $\Delta E^{\ddagger}_{eff}$ (B3/B1a), for the **1**-L$_{ax}$ oxidants series, now follows the experimental trends. Thus, as can be seen from entry (b) in Table 1, **1**-(CH$_2$)$_2$S$^-$ possesses the lowest effective barrier toward **S2**(DHA), followed by **1**-N$_3^-$, while the electrophilic oxidant **1**-AN displays the highest barrier/free energy barrier. The free energy barrier difference for **1**-(CH$_2$)$_2$S$^-$ versus **1**-AN is −1.5 kcal/mol in good accord with the experimental difference of −2.0 kcal/mol.[10] The lower barrier for the reaction of **1**-(CH$_2$)$_2$S$^-$ with **S2** (DHA) is reproduced by all of the functionals tried (Supporting Information Table S8), while the UB3LYP result in Table 1 has the best fit to the experimental data.

Consideration of entries (a) in Table 1 shows, however, that with **S1** (CHD) the behavior is different. Now, despite the larger $\Delta\Delta E^{\ddagger}_{tun}$ correction for **1**-(CH$_2$)$_2$S$^-$, the effective free energy barriers for **1**-(CH$_2$)$_2$S$^-$ and **1**-AN are very close. Testing these two reactions with other functionals (Supporting Information Table S8) reinforces the conclusion of Table 1, that the

Figure 6. Tunneling trends: (a) A plot of tunneling correction of the barrier versus the electron donation index Δq_{CT} of the axial ligand. (b) A plot of the transmission coefficients for H tunneling, κ_H, versus Δq_{CT}. (c) A plot of the imaginary frequency in the TS, $\nu_H^{\ddagger}$, versus Δq_{CT}. Energies are in kcal mol^{-1} and ν_H is in i cm^{-1}.

tunneling-corrected effective free energy barriers (and hence also the rate constants) for the reactions of **1**-AN and **1**-(CH$_2$)$_2$S$^-$ with CHD are either close to one another or favoring **1**-AN. Because CHD was studied experimentally only in combination with **1**-AN,[10] this is a prediction to be tested by experiment.

Table 2. Tunneling Correction Values ($\Delta\Delta E^{\ddagger}_{tun}$, in kcal mol^{-1}) at 273 K for H-Abstraction from S1 (CHD) and S2 (DHA) by 1-AN and 1-(CH$_2$)$_2$S$^-$, Calculated Using Different Levels of Single-Point Energy and Solvation Corrections (Solvent Models in Parentheses) on the UB3LYP/B1a Geometries of Reactants and TS for the S = 2 Process

substrate	oxidant	UB3LYP[a] (PBS)	UB3LYP[b] (SMD)	UM06L[b] (SMD)	UOPBE[b] (SMD)	UTPSSH[b] (SMD)	UTPSSh[c] (SMD)
S1	**1**-AN	1.4	1.4	0.9	1.5	1.5	2.0
	1-(CH$_2$)$_2$S$^-$	3.4	3.4	2.3	3.4	3.4	3.2
S2	**1**-AN	1.5	1.5	0.7	1.4	1.5	[d]
	1-(CH$_2$)$_2$S$^-$	3.5	3.4	2.0	3.1	3.5	[d]

[a]UB3LYP/B3//UB3LYP/B1a; PBS is the Poisson−Boltzmann solvation model. [b]Functional (solvent model) B3//UB3LYP/B1a calculations. [c]TPSSh(SMD)/B3//TPSSH/B1a calculations. [d]TPSSH optimization has been performed only for **S1**.
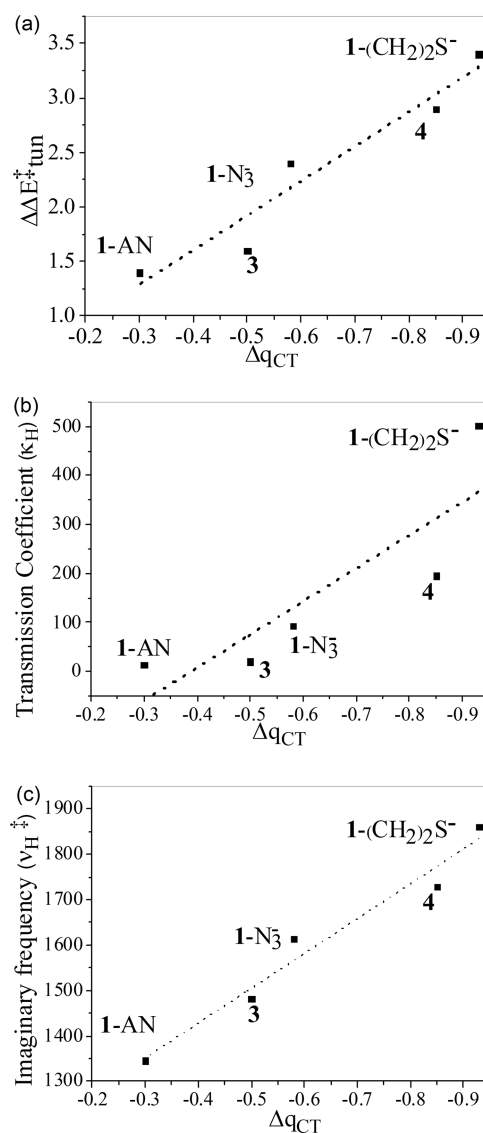
Further comparison of the tunneling-corrected barriers of **1**-AN, **3**, and **4** in Table 1 shows that they follow the experimental trend[18] and decrease in the following order, **4** > **3** ≥ **1**-AN. The largest barrier for **4** reflects the interplay of a few factors: (i) the substantial energy difference, ΔE_{TQ}, between the triplet ground state and the reactive quintet state of the oxidant (Figure 2), and the strong electron donation effect of the axial ligand, both which raise the LUMO and increase the classical barrier to begin with; and (ii) the tunneling correction, $\Delta\Delta E^{\ddagger}_{tun}$, while substantial (2.9 kcal mol^{-1}) is still not sufficiently large to lower the effective barrier below those of the other oxidants.

Thus, all in all, tunneling appears to control all of the observed trends of H-abstraction reactivity of **1**-L$_{ax}$ oxidants with **S1** and **S2**. At the same time, we cannot rule out that different spin inversion probabilities (SIP)[56] of **1**-AN and **1**-(CH$_2$)$_2$S$^-$ may go hand-in-hand with the tunneling effect.[10,11] Thus, while the MECP for **1**-(CH$_2$)$_2$S$^-$ is energetically very low, thus presumably leading to large spin−orbit coupling (SOC) and efficient spin pre-equilibrium, the corresponding MECP of **1**-AN is relatively high (Supporting Information Figure S7),[13b] thus having presumably smaller SIP, which further contributes to a higher effective barrier for H-abstraction.

To comprehend the trend in the $\Delta\Delta E^{\ddagger}_{tun}$ quantities (in entries (a) and (b)), let us inspect the transmission coefficients (κ_H) in Table 1. These κ_H coefficients are quite large (also for D, see Table 3 later) for all of the reactions. The values are particularly large for the reactions of **1**-(CH$_2$)$_2$S$^-$ and substantially smaller for **1**-AN, and generally follow the electron donation power of the axial ligand. Figure 6b shows this trend pictorially. As further shown in Figure 6c, the transmission coefficient increases with the increase in the imaginary frequency of the TS, $\nu_H^{\ddagger}$. It is seen that **1**-(CH$_2$)$_2$S$^-$ with the highest imaginary frequency has the largest transmission coefficient for H tunneling, while **1**-AN with the lowest imaginary frequency has the smallest transmission coefficient. This trend matches the electron-donating power of the axial ligand.

To further comprehend the trend in the transmission coefficients in the series, we note that the tighter TS with the shortest O---H---C distance is **1**-(CH$_2$)$_2$S$^-$, while the loosest one with the longest distance is the TS for **1**-AN. These trends in the imaginary frequency and the TS tightness mean that what controls the value of the transmission coefficient is the width of the barrier;[19,36,39,41b] the sharper is the potential energy barrier, the larger is the tunneling effect.[57] To illustrate the barrier-width effect, we show in Figure 7 the quintet potential energy profiles for the H-abstraction reactions of **1**-AN and **1**-(CH$_2$)$_2$S$^-$. It is seen that **1**-AN exhibits a flat wide barrier, whereas **1**-(CH$_2$)$_2$S$^-$ possesses a rather sharp barrier in the transition state region, in the range from −2.75 to +0.75 units of the IRC. The other reactions also follow this trend, showing that the width of the barrier decreases with the increase of the donor ability of the axial ligand. The corresponding plots of the energy barriers versus IRCs are shown in the Supporting Information (Figure S8).

Predictions of Kinetic Isotopic Effects. Kinetic isotope effect (KIE) is a mechanistic phenomenon that can provide useful information about the rate-determining step as well as the presence of tunneling. Because KIE values were experimentally measured,[10] for some H-abstraction reactions of **1**-L$_{ax}$ oxidants, we sought to verify our tunneling results by calculating KIEs and comparing them with the experimental data where available. Thus, to verify the proposed tunneling effect, we computed the kinetic isotopic effect.
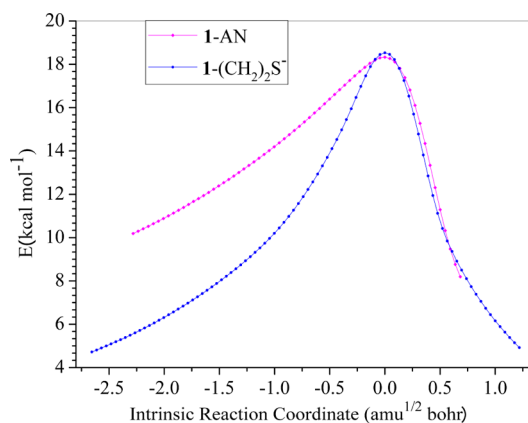

Figure 7. Potential energy (E, in kcal mol^{-1}) versus intrinsic reaction coordinate (in amu$^{1/2}$ bohr) for H-abstraction from **S1** at $S = 2$ by **1**-AN and **1**-(CH$_2$)$_2$S$^-$ computed at the UB3LYP/B1a level of theory.

Table 3. Comparison of the Calculated and Experimental KIE Values (k_H/k_D) at 298 K

reaction	κ_H/κ_D [a]	KIE$_{Ey}$/KIE$_W$ [b]	KIE$_{ECK}$ [c]	KIE$_{EXP}$
(a) $S = 2$ (CHD)				
1-AN	8.3/3.9	5.7/7.5	12.2	
1-(CH$_2$)$_2$S$^-$	143.6/16.6	5.9/8.7	51	
3	11.8/4.6	5.4/7.5	14	
4	65.7/11.0	4.5/6.3	26	
(b) $S = 2$ (DHA)				
1-AN	9.5/3.8	5.8/7.8	14.4 (10.3)	10
1-(CH$_2$)$_2$S$^-$	162.5/15.8	5.6/8.4	58(46)	
1-N$_3$$^-$	36/7.2	5.0/7.2	25.3	17
(c) $S = 1$ (CHD)				
1-AN	2932/61	1.1/1.7	54	
1-(CH$_2$)$_2$S$^-$	7613/89	4.7/7.1	398	
3	2786/51	5.9/8.9	322	
4	7104/88	3.2/4.9	259	

[a]κ_H/κ_D stands for the transmission coefficients of H followed by D at 298 K. [b]KIE values are given in the order of Eyring/Wigner corrected at the B3//B1a level. [c]Eckart corrected KIE value at B3//B1a and the data given in parentheses are B3//B1b values.

Table 3 collects KIE values calculated with the Eyring equation followed by Wigner corrected ones. In the second column, we show the Eckart-based transmission coefficient ratios, κ_H/κ_D, with the value for H being followed by that of D. The next two columns show tunneling corrected KIEs and experimental values.[10] The semiclassical Eyring KIE$_{Ey}$ values are seen to cluster between 4.5 and 5.9. The Wigner corrected values KIE$_W$ increase slightly these values to 6.3−8.7, while the Eckart, KIE$_{ECK}$, values are much larger, ranging from 12 to 58 for $S = 2$. For **1**-AN and **1**-N$_3$$^-$ where experimental KIE$_{EXP}$ data are available the Eckart corrected KIE values are seen to match, reasonably well, with the available experimental values. This match confirms the presence of tunneling and suggests the reliability of the Eckart method.

The last part (c) of Table 3 shows in boldface the putative KIE$_{ECK}$ values for the H-abstraction reactions were they to transpire on the triplet state ($S = 1$) surface. It is seen that these values are large (KIE$_{ECK}$ = 54−398), and hugely different from the experimental values of 10−17. The same applies to the KIE values calculated with the UTPSSh functional (see Supporting Information Table S7). This is an indirect evidence that the reaction transpires on the quintet-state surface and hence a

strong support of TSR.[58] Furthermore, these results imply that KIE is a probe of the reactive spin state, as argued before.[59−61]

The data in Table 3 make an additional prediction, that KIE_{ECK} values increase with the electron donation power of the axial ligand. Figure 8 shows this trend pictorially, and it is seen that the
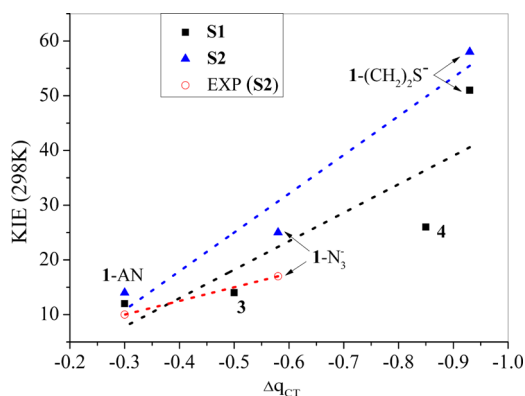

Figure 8. Relationship between kinetic isotopic effect at 298 K with the charge transfer, Δq_{CT}, from the axial ligand to the rest of the complex. "■" and blue "▲" are computed data of S = 2 for **S1** and **S2**, respectively, while red "○" are experimental data. The dashed lines serve to guide the eye.

only available experimental KIE values (red circles) follow this trend. Therefore, it is predicted that the experimental KIE value for **1**-$(CH_2)_2S^-$ should be in the range of 50, which is close to the datum for the nonheme enzyme TauD abstracting an H atom from α-Taurine.[1,62] Similarly, the experimental KIE for the reaction of **4** with CHD should be in the range of 20, while for **3** with CHD, the value should be similar to the one measured for **1**-AN + DHA. These predictions can test the TSR and tunneling hypothesis presented here.

Other Antielectrophilic Reactivity Trends of Iron(IV)−Oxo Reagents. The above results show that the antielectrophilic reactivity trend of **1**-L_{ax} oxidants in H-abstraction from two substrates (**S1** and **S2**) derives from tunneling that increases as the axial ligand becomes a better electron donor. This clear conclusion could have been deduced because the BEP effect is not important in the **1**-L_{ax} series, wherein the $BDE_{O−H}$ is constant and independent of the axial ligand.

There are, however, other antielectrophilic reactivity patterns in the literature, which may or may not belong to the same category as the present systems (this will require tunneling calculations). Such a series is the axially substituted iron(IV)−oxo porphyrin radical cation complexes,[15] wherein the H-abstraction barriers were found to decrease as the electron-donating power of the axial ligand increased. As was shown by theoretical calculations,[15] when the axial ligand were anions, such as $CF_3SO_3^-$, Cl^-, and CH_3COO^-, the O−H bond that is formed by H-abstraction was getting stronger as the axial ligand was made a better electron donor. Thus, the antielectrophilicity trend in this series was interpreted to reflect the BEP principle.[15] However, a recent study by Fuji et al.,[63a] of related iron(IV)−oxo porphyrin radical cation complexes with different axial ligands, showed tunneling that increases as the axial ligand changes from the neutral imidazole to the anionic Cl^- and NO_3^- ligands. A similar report by Newcomb et al.,[63b] of iron(IV)−oxo porphyrin radical cations with different porphyrin substituents, exhibits high KIE values that were found to depend on the porphyrin substituents, such that electron donor substituents led to

significantly higher values than electron-withdrawing substituents. Thus, when both tunneling and BEP effects conspire, separating the two effects may be difficult but not impossible. First, KIE measurements and their temperature dependence are capable of revealing the role of tunneling as in the above two studies,[63] and, second, theoretical calculations as done here can reveal the BEP as well as the KIE effects. This interplay of experiment and theory can reveal more generally the role of tunneling in shaping reactivity and selectivity patterns.

Another antielectrophilic trend was reported for $[Fe^{IV}(O)(L^8Py_2)(PyO_{ax})]^{2+}$ where the axial ligand was *para*-substituted pyridine *N*-oxide (PyO_{ax}).[64] It is likely that the O−H bond strength in the latter series is only weakly dependent on the identity of the axial ligand, and, if so, the trend may reflect axial-ligand-dependent tunneling. However, the findings[64] that the same series exhibits an antielectrophilic reactivity trend also for O-transfer reactions indicate that the scenario is more complex and it may involve also a variable triplet−quintet energy gap, ΔE_{TQ} (Figure 1), that affects the relative reactivity, as in the analogous heme series.[15]

■ CONCLUSION

In response to a recent challenge,[18] we looked afresh at the hydrogen-abstraction (H-abstraction) and oxygen-transfer (O-transfer) reactivity of a series of nonheme $[Fe^{IV}(O)(TMC)(L_{ax})]^{2+}$ complexes[10,18] (Scheme 1), with a tetramethyl cyclam ligand and different axial ligands (L_{ax}), toward three substrates: 1,4-cyclohexadiene (CHD), 9,10-dihydroanthracene (DHA), and triphenyl phosphine (PPh_3) (Scheme 2). The motivation for undertaking this study were the findings[10] that while the O-transfer reactivity followed nicely the relative electrophilicity of the complexes, by contrast the corresponding H-abstraction reactivity, for one group of the complexes (**1**-L_{ax}, Scheme 2), was counterintuitive and found to increase as the axial ligand became a better electron donor, hence an antielectrophilic trend.

Our results show that tunneling at 273 K controls the antielectrophilic trend in H-abstraction, by slicing more of the corresponding reaction barrier as the axial ligand is made a better electron donor (Scheme 5; Tables 1 and 2). While the contribution of spin inversion probabilities to this trend[10,11,13,56] cannot be dismissed, and will have to be tested eventually by state-of-the-art calculations and theory, it is very clear from the study that this variation of the tunneling reverses the natural electrophilic trend (as revealed through calculations without tunneling). At the same time, the O-transfer reactivity, which is not subject to tunneling, retains an electrophilic-dependent reactivity trend, as revealed by experiment and computations.

Using kinetic isotope effect (KIE) calculations with tunneling, we were also able to show that a match to the experimental KIE values can be achieved only if all of the H-abstraction reactions proceed on the quintet state (S = 2) surface. The KIE values on the triplet (S = 1) are much too large (Table 3) to match experiment. As such, the present results corroborate the initially predicted two-state reactivity (TSR) scenario for these reactions.[10,11,13−16] Our study predicts also KIEs for reactions of, for example, **1**-$(CH_2)_2S^-$, **3**, and **4**, etc., which can be tested by experiment to verify or falsify the role of tunneling.

These key findings clarify the long-standing puzzle posed by the reactivity trends of these complexes. Furthermore, the qualitative relation of tunneling with the electron releasing tendency of the ligands provides support for the "tunneling control" hypothesis of Schreiner et al.[19] Further effort to

calculate more precise and rigorous multidimensional tunneling may provide additional insight about the importance of hydrogen tunneling in chemical reactivity. Testing our predicted KIE values for the 1-L_{ax} and 2–4 oxidants is possible and required. Should the predictions be corroborated by experiment, the entire field of C–H bond activation in bioinorganic chemistry would lay open to reinvestigation.

■ ASSOCIATED CONTENT

Ⓢ Supporting Information

Full citation of Gaussian 09, energy profiles, geometries, orbital pictures (Figures S1–S17), absolute energies, Mulliken spin and charges (Tables S1–S17), and optimized Cartesian coordinates for all of the stationary points. This material is available free of charge via the Internet at http://pubs.acs.org.

■ AUTHOR INFORMATION

Corresponding Author

sason@yfaat.ch.huji.ac.il

Present Addresses

†Department of Lipid Science, CSIR-Central Food Technological Research Institute, Mysore 570 020, India.
‡Department of Chemistry, School of Mathematical and Physical Sciences, Central University of Kerala, Kerala 671 314, India.

Notes

The authors declare no competing financial interest.

■ ACKNOWLEDGMENTS

■ REFERENCES

(1) Krebs, C.; Galonić-Fujimori, D.; Walsh, C. T.; Bollinger, J. M., Jr. *Acc. Chem. Res.* **2007**, *40*, 484–492.
(2) Que, L., Jr. *Acc. Chem. Res.* **2007**, *40*, 493–500.
(3) Nam, W. *Acc. Chem. Res.* **2007**, *40*, 522–531.
(4) Shan, X.; Que, L., Jr. *J. Inorg. Biochem.* **2006**, *100*, 421–433.
(5) Lacy, D. C.; Gupta, R.; Stone, K. L.; Greaves, J.; Ziller, J. W.; Hendrich, M. P.; Borovik, A. S. *J. Am. Chem. Soc.* **2010**, *132*, 12188–12190.
(6) Nam, W.; Lee, Y.-M.; Fukuzumi, S. *Acc. Chem. Res.* **2014**, *47*, 1146–1154.
(7) de Visser, S. P. *J. Am. Chem. Soc.* **2010**, *132*, 1087–1097.
(8) Borovik, A. S. *Chem. Soc. Rev.* **2011**, *40*, 1870–1874.
(9) Saouma, C. T.; Mayer, J. M. *Chem. Sci.* **2014**, *5*, 21–31.
(10) Sastri, C. V.; Lee, J.; Oh, K.; Lee, Y. J.; Lee, J.; Jackson, T. A.; Ray, K.; Hirao, H.; Shin, W.; Halfen, J. A.; Kim, J.; Que, L., Jr.; Shaik, S.; Nam, W. *Proc. Natl. Acad. Sci. U.S.A.* **2007**, *104*, 19181–19186.
(11) Hirao, H.; Que, L., Jr.; Nam, W.; Shaik, S. *Chem.—Eur. J.* **2008**, *14*, 1740–1756.
(12) Usharani, D.; Lacy, D. C.; Borovik, A. S.; Shaik, S. *J. Am. Chem. Soc.* **2013**, *135*, 17090–17104.
(13) (a) Hirao, H.; Kumar, D.; Que, L., Jr.; Shaik, S. *J. Am. Chem. Soc.* **2006**, *128*, 8590–8606. (b) Usharani, D.; Janardanan, D.; Li, C.; Shaik, S. *Acc. Chem. Res.* **2013**, *46*, 471–482.
(14) Poli, R.; Harvey, J. N. *Chem. Soc. Rev.* **2003**, *32*, 1–8.
(15) Kang, Y.; Chen, H.; Jeong, Y. J.; Lai, W.; Bae, E. H.; Shaik, S.; Nam, W. *Chem.—Eur. J.* **2009**, *15*, 10039–10046.
(16) Shaik, S.; Chen, H.; Janardanan, D. *Nat. Chem.* **2011**, *3*, 19–27.
(17) Dhuri, S. N.; Seo, M. S.; Lee, Y. M.; Hirao, H.; Wang, Y.; Nam, W.; Shaik, S. *Angew. Chem. Int., Ed.* **2008**, *47*, 3356–3359.
(18) England, J.; Bigelow, J. O.; Heuvelen, K. M. V.; Farquhar, E. R.; Martinho, M.; Meier, K. K.; Frisch, J. R.; Munck, E.; Que, L., Jr. *Chem. Sci.* **2014**, *5*, 1204–1215.

(19) (a) Ley, D.; Gerbig, D.; Schreiner, P. R. *Org. Biomol. Chem.* **2012**, *10*, 3781–3790. (b) Schreiner, P. R.; Reisenauer, H. P.; Ley, D.; Gerbig, D.; Wu, C.-H.; Allen, W. D. *Science* **2011**, *332*, 1300–1303.
(20) Janardanan, D.; Usharani, D.; Chen, H.; Shaik, S. *J. Phys. Chem. Lett.* **2011**, *2*, 2610–2617.
(21) Johansson, A. J.; Blomberg, M. R.; Siegbahn, P. E. M. *J. Phys. Chem. C* **2007**, *111*, 12397–12406.
(22) Becke, A. D. *J. Chem. Phys.* **1992**, *96*, 2155–2160.
(23) Becke, A. D. *J. Chem. Phys.* **1993**, *98*, 5648–5652.
(24) Lee, C.; Yang, W.; Parr, R. G. *Phys. Rev. B* **1988**, *37*, 785–789.
(25) Hay, J. P.; Wadt, W. R. *J. Chem. Phys.* **1985**, *82*, 299–310.
(26) Friesner, R. B.; Murphy, R. B.; Beachy, M. D.; Ringlanda, M. N.; Pollard, W. T.; Dunietz, B. D.; Cao, Y. X. *J. Phys. Chem. A* **1999**, *103*, 1913–1928.
(27) Schafer, A.; Horn, H.; Ahlrichs, R. *Chem. Phys.* **1992**, *97*, 2571–2577.
(28) *Jaguar, Version 7.6*; Schrödinger, LLC: New York, NY, 2008.
(29) Frisch, M. J.; et al. *Gaussian 09*, revision D.01; Gaussian, Inc.: Pittsburgh, PA, 2009. Full citations are available in the Supporting Information.
(30) Schafer, A.; Huber, C.; Ahlrichs, R. *J. Chem. Phys.* **1994**, *100*, 5829–5835.
(31) Marten, B.; Kim, K.; Cortis, C.; Friesner, R. A.; Murphy, R. B.; Ringnalda, M. N.; Sitkoff, D.; Honig, B. *J. Phys. Chem.* **1996**, *100*, 11775–11778.
(32) (a) Tao, J. M.; Perdew, J. P.; Staroverov, V. N.; Scuseria, G. E. *Phys. Rev. Lett.* **2003**, *91*, 146401. (b) Zhao, Y.; Truhlar, D. G. *J. Chem. Phys.* **2006**, *125*, 194101-1–18. (c) Cohen, A. J.; Handy, N. C. *Mol. Phys.* **2001**, *99*, 607–615. (d) Perdew, J. P.; Burke, K.; Ernzerhof, M. *Phys. Rev. Lett.* **1996**, *77*, 3865–3868. (e) Marenich, A. V.; Cramer, C. J.; Truhlar, D. G. *J. Phys. Chem. B* **2009**, *113*, 6378–6396.
(33) Grimme, S. *J. Comput. Chem.* **2006**, *27*, 1787–1799.
(34) (a) Truhlar, D. G.; Garrett, B. C. *Acc. Chem. Res.* **1980**, *13*, 440–448. (b) Klippenstein, S. J.; Pande, V. S.; Truhlar, D. G. *J. Am. Chem. Soc.* **2014**, *136*, 528–546.
(35) Truhlar, D. G.; Kuppermann, A. *J. Am. Chem. Soc.* **1971**, *93*, 1840–1851.
(36) Maity, D. K.; Bell, R. L.; Truong, T. N. *J. Am. Chem. Soc.* **2000**, *122*, 897–906.
(37) Zhang, F.; Dibble, T. S. *Phys. Chem. Chem. Phys.* **2011**, *13*, 17969–17977.
(38) Vandeputte, A. G.; Sabbe, K. M.; Reyniers, M. F.; Speybroeck, V. V.; Waroquier, M.; Marin, G. B. *J. Phys. Chem. A* **2007**, *111*, 11771–11786.
(39) Dybala-Defratyka, A.; Paneth, P.; Banerjee, R.; Truhlar, D. G. *Proc. Natl. Acad. Sci. U.S.A.* **2007**, *26*, 10774–10779.
(40) Duncan, W. T.; Bell, R. L.; Truong, T. N. *J. Comput. Chem.* **1998**, *19*, 1039–1052.
(41) (a) Eckart, C. *Phys. Rev.* **1930**, *35*, 1303–1309. (b) See also: Truong, T. N.; Truhlar, D. G. *J. Chem. Phys.* **1990**, *93*, 1761–1769.
(42) Eyring, H. *J. Chem. Phys.* **1935**, *3*, 107–115.
(43) Wigner, E. *J. Chem. Phys.* **1937**, *5*, 720–725.
(44) Rohde, J. U.; In, J. H.; Lim, M. H.; Brennessel, W. W.; Bukowski, M. R.; Stubna, A.; Munck, E.; Nam, W.; Que, L., Jr. *Science* **2003**, *299*, 1037–1039.
(45) Geng, C.; Ye, S.; Neese, F. *Angew. Chem., Int. Ed.* **2010**, *49*, 5717–5720.
(46) Neidig, M. L.; Decker, A.; Choroba, O. W.; Huang, F.; Kavana, M.; Moran, G. R.; Spencer, J. B.; Solomon, E. I. *Proc. Natl. Acad. Sci. U.S.A.* **2006**, *103*, 12966–12973.
(47) Decker, A.; Rohde, J.-U.; Klinker, E. J.; Wong, S. D.; Que, L., Jr.; Solomon, E. I. *J. Am. Chem. Soc.* **2007**, *129*, 15983–15996.
(48) de Visser, S. P. *J. Am. Chem. Soc.* **2006**, *128*, 9813–9824.
(49) Bernasconi, L.; Louwerse, M. J.; Baerends, E. J. *Eur. J. Inorg. Chem.* **2007**, 3023–3033.
(50) Ye, S.; Neese, F. *Curr. Opin. Chem. Biol.* **2009**, *13*, 89–98.
(51) Shengfa, Y.; Cai-Yun, G.; Shaik, S.; Neese, F. *Phys. Chem. Chem. Phys.* **2013**, *15*, 8017–8030.

(52) Janardanan, D.; Wang, Y.; Schyman, P.; Que, L., Jr.; Shaik, S. *Angew. Chem., Int. Ed.* **2010**, *49*, 3342−3345.

(53) (a) Chen, H.; Lai, W. Z.; Shaik, S. *J. Phys. Chem. Lett.* **2010**, *1*, 1533−1540. (b) A recent extensive benchmark for a model H-abstraction reaction of an iron−oxo reagent shows that the B3LYP functional performs the best among the functional and its results are virtually as good as those of CCSD(T)/CBS values. See: Altun, A.; Breidung, J.; Neese, F.; Thiel, W. *J. Chem. Theory Comput.* **2014**, *10*, 3807−3820.

(54) Bell, R. P. *Proc. R. Soc. London, Ser. A* **1936**, *154*, 414−429.

(55) Evans, M. G.; Polanyi, M. *Trans. Faraday Soc.* **1938**, *34*, 11−14.

(56) Cho, K. B.; Chen, H.; Janardanan, D.; de Visser, S. P.; Shaik, S.; Nam, W. *Chem. Commun.* **2012**, *48*, 2189−2191.

(57) Inagaki, T.; Yamamoto, T. *J. Phys. Chem. B* **2014**, *118*, 937−950.

(58) Schröder, D.; Shaik, S.; Schwarz, H. *Acc. Chem. Res.* **2000**, *33*, 139−145.

(59) Li, C.; Wu, W.; Kumar, D.; Shaik, S. *J. Am. Chem. Soc.* **2006**, *128*, 394−395.

(60) Wang, W.; Kumar, D.; Yang, C.; Han, K.; Shaik, S. *J. Phys. Chem. B* **2007**, *111*, 7700−7710.

(61) Harris, N.; Shaik, S.; Schröder, D.; Schwarz, H. *Helv. Chim. Acta* **1999**, *82*, 1784−1797.

(62) Price, C. J.; Barr, E. W.; Glass, T. E.; Krebs, C.; Bollinger, J. M., Jr. *J. Am. Chem. Soc.* **2003**, *125*, 13008−13009.

(63) (a) Cong, Z.; Kinemuchi, H.; Kurahashi, T.; Fuji, H. *Inorg. Chem.* **2014**, *53*, 10632−10641. (b) Pan, Z.; Horner, J. H.; Newcomb, M. *J. Am. Chem. Soc.* **2008**, *130*, 7776−7777.

(64) Zhou, Y.; Shan, X.; Mas-Balleste, R.; Bukowski, M. R.; Stubna, A.; Chakrabarti, M.; Slominski, L.; Halfen, J. A.; Munck, E.; Que, L., Jr. *Angew. Chem., Int. Ed.* **2008**, *47*, 1896−1899.